Science Advances

AAAS

advances.sciencemag.org/cgi/content/full/4/6/eaat7189/DC1

Supplementary Materials for

Ultra-confined mid-infrared resonant phonon polaritons in van der Waals nanostructures

Michele Tamagnone, Antonio Ambrosio, Kundan Chaudhary, Luis A. Jauregui, Philip Kim, William L. Wilson, Federico Capasso

Published 15 June 2018, *Sci. Adv.* **4**, eaat7189 (2018)
DOI: 10.1126/sciadv.aat7189

The PDF file includes:

- section S1. PiFM and s-SNOM schematics
- section S2. Fringing field correction
- section S3. Modeling of resonators fields, light path contributions, and their separation
- section S4. Additional measurements
- section S5. Numerical simulations of Purcell factors
- fig. S1. PiFM and s-SNOM schematics.
- fig. S2. Possible light paths and coupling coefficients.
- fig. S3. Additional PiFM image of the dipole antenna.
- fig. S4. Polaritons in discs and ellipses in the RS1 band.
- fig. S5. Comparison of PiFM and s-SNOM on the same setup (Neaspec).
- fig. S6. Resonance in a disc shifted from its original position.
- fig. S7. Monochromatic PiFM images.
- table S1. Purcell factors for nanodiscs.
- table S2. Purcell factors for nanoantennas.
- Legends for movies S1 to S4

Other Supplementary Material for this manuscript includes the following:
(available at advances.sciencemag.org/cgi/content/full/4/6/eaat7189/DC1)

- movie S1 (.mp4 format). Hyperspectral PiFM for different wavelengths in the RS1 band.
- movie S2 (.mp4 format). Hyperspectral PiFM for different wavelengths in the RS2 band.

- movie S3 (.mp4 format). Zoom-in hyperspectral PiFM for different wavelengths in the RS1 band.
- movie S4 (.mp4 format). Zoom-in hyperspectral PiFM for different wavelengths in the RS2 band.

section S1. PiFM and s-SNOM schematics

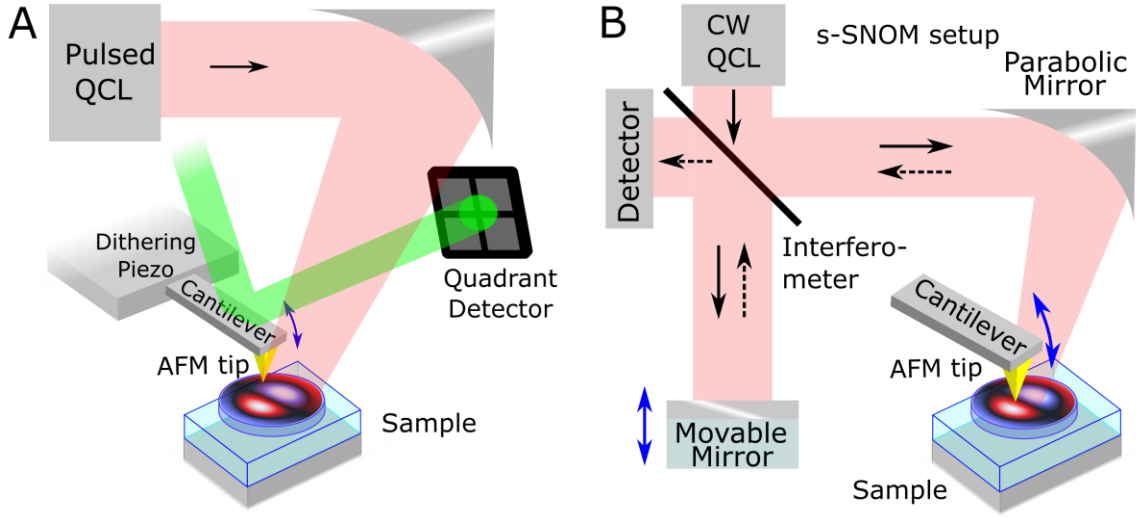

fig. S1. PiFM and s-SNOM schematics. (**A**) PiFM (Molecular Vista) setup: a pulsed laser is focused on an AFM tip, operating in tapping mode with the the second cantilever resonance mode (about 1.8MHz oscillation frequency). The repetition rate of the pulsed QCL is tuned to match the frequency difference between the first and second mechanical eigenmode of the AFM cantilever. The cantilever first eigenmode is then used for the readout. An optical force is created between the sample and the AFM under illumination, and its effect is monitored directly from the cantilever oscillation. No optical detector is used in this type of measure, that is in fact *photon-less*. (**B**) The s-SNOM setup uses a continuous wave QCL laser to illuminate the sample and the tip. An interferometer with a pseudoheterodyne detection is used to extract the phase and the amplitude of the scattered signal. Light is p-polarized in both setups.

section S2. Fringing field correction

As specified in the main paper, the 2D wave equation for the modes in the RS2 band is

$$(i\omega)^2\rho = v_p^2(\omega)\nabla^2\rho \tag{S1}$$

As the charge density ρ oscillates with time, a surface displacement current $\boldsymbol{J}$ is created, which is related to ρ by the continuity equation

$$\nabla \cdot \boldsymbol{J} = -(i\omega)\rho \tag{S2}$$

Combining these equations, we find

$$-i\omega\nabla \cdot \boldsymbol{J} = v_p^2(\omega)\nabla \cdot (\nabla\rho) \tag{S3}$$

Except for a spatially uniform term (which is unphysical in this finite size problem), equation S3 implies

$$\boldsymbol{J} = -\frac{v_p^2(\omega)}{i\omega}\nabla\rho \tag{S4}$$

Note that we are assuming that the current density has no curl, and that it is due only to the displacement of the charge density. At the edges of the patterned flake, the component of $\boldsymbol{J}$ orthogonal to the edge must vanish, and hence we obtain the Neumann boundary condition on the spatial derivative of ρ, which for a circle with radius a reads

$$\left.\frac{\partial\rho}{\partial r}\right|_{r=a} = 0 \tag{S5}$$

Solving the 2D wave equations in a circular domain always leads to solutions expressed using Bessel functions, with solution prototype

$$\rho = J_s(kr)(A\cos(s\theta) + B\sin(s\theta))e^{i\omega t} \tag{S6}$$

where $\omega = v_p k$ and J_s is the Bessel function of order s. The boundary condition in (S5) gives

$$\rho = J_s(k_{sn}r)(A\cos(s\theta) + B\sin(s\theta))e^{i\omega t} \text{ where } k_{sn} \text{ is the n}^{\text{th}} \text{ root of } J_s'(ka) = 0 \tag{S7}$$

The resonant wave vector k_{sn} then determines the resonant frequency via $\omega_{sn} = v_p k_{sn}$, where $s = 0,1,2,$ ... and $n = 1,2,3$ ....

The solution for $s = 0, n = 1$ is the constant solution, which represents the total charge, which we assume to be 0 by charge neutrality, hence we can disregard this case.

As explained in (*16*) and (*19*), this ideal boundary condition does not consider the fringing fields, i.e. the electric field appearing beyond the edge of the flake when a mode propagating towards the edge is reflected by it. Both references (*19*) and (*21*) have studied this effect in detail. Due to the energy stored in the fringing fields, the reflected wave experiences an extra phase shift, which in our case is determined with fitting. The phase factor ϕ is added directly in the Bessel function in the equation as

$$\rho = J_s(k_{sn}r + \phi)(A\cos(s\theta) + B\sin(s\theta))e^{i\omega t} \text{ where } k_{sn} \text{ is the n}^{\text{th}} \text{ root of } J_s'(ka + \phi) = 0 \tag{S8}$$

The value of ϕ which ensures the best agreement between measured and analytical prediction is -0.28π in our case, in close agreement with the value -0.25 π found for both graphene in (*19*) and h-BN (*21*). Notice that in (*19*) and (*21*) the sign of the phase factor is different due to the use of the $e^{-i\omega t}$ physics time harmonic convention, while in this work we use the $e^{i\omega t}$ engineering time harmonic convention, which agrees with the canonical definition of the Fourier transform.

If $s = 0$ the sine term vanishes and only one mode (radially symmetric) for each n is found. If $s \geq 1$ then

for each n two degenerate solutions are found, and any linear combination via the complex coefficients A, B can be used. Because the solutions are degenerate, several choices of the basis are possible. One way is to use the $\{\cos(s\theta), \sin(s\theta)\}$ pair, giving modes oriented at different angles, so that nodes and antinodes are exchanged. With this representation, for $s = 1, n = 1$ the fundamental dipole modes observed experimentally are found. Alternatively, since A and B can be chosen as complex numbers, also the pair $\{e^{is\theta}, e^{-is\theta}\}$ can be selected. In this way, the presence of the degenerate modes can be represented directly as the sign of s, which is then interpreted as the angular momentum topological charge of the modes.

section S3. Modeling of resonators fields, light path contributions, and their separation

To interpret the s-SNOM and PiFM images and to analyze quantitatively the light paths contributions, we provide here a model of the fields associated with the resonant modes. For simplicity, we do not consider here the substrate, the presence of which does not affect the conclusions of this argument but merely the geometry of the radiated fields. First, assuming that the resonator is driven by a monochromatic source at the resonant frequency, the fields surrounding the resonator can be found from the displacement currents in h-BN with the radiation integral for the vector potential $\boldsymbol{A_R}$

$$\boldsymbol{A_R}(r) = \frac{\mu_0}{4\pi} \iiint_V \boldsymbol{J_R}(r') \frac{e^{-ik|r-r'|}}{|r-r'|} \mathrm{d}^3 r' \tag{S9}$$

where $k = \omega/c$ and the subscript $\boldsymbol{R}$ indicates that the fields are associated to the resonance. The electric field is given by

$$\boldsymbol{E_R} = -i\omega \boldsymbol{A_R} + \frac{1}{i\omega\mu_0\varepsilon_0} \nabla(\nabla \cdot \boldsymbol{A_R}) \tag{S10}$$

If the h-BN resonator is much smaller than the wavelength, then equation S9 can be approximated with

$$\boldsymbol{A_R}(r) \simeq \frac{\mu_0}{4\pi} \frac{e^{-ik|r|}}{|r|} \iiint_V \boldsymbol{J_R}(r') \, \mathrm{d}^3 r' \tag{S11}$$

For nano-discs, from simple symmetry arguments, it is seen that the only modes that can radiate (bright modes) must have $s = \pm 1$, since for other values of s it is possible to split the integral on two halves of the disc giving opposite contributions that cancel each other.

Let us now go back to a general h-BN nanoparticle (much smaller than the wavelength), and we consider the impulse response. In other words, we assume that energy is instantaneously coupled in the mode at the instant $t = 0$, and we observe the time domain fields dynamics. The considered resonant modes have quality factors in the order of 100 or more, hence all the associated fields ($\boldsymbol{E_R}, \boldsymbol{H_R}, \boldsymbol{A_R}, \boldsymbol{J_R}, \rho_R$) show damped oscillations. In the near field of the dipole the propagation delay can be neglected since the fields are quasi-static

$$\boldsymbol{E_R}, \boldsymbol{H_R}, \boldsymbol{A_R}, \boldsymbol{J_R}, \rho_R \propto \mathrm{u}(t)\cos(\omega_0 t + \alpha)\, e^{-\gamma t} \tag{S12}$$

where $\mathrm{u}(t)$ is the unit step function, ω_0 is the resonance frequency, and γ is the damping coefficient. The resonance quality factor is then given by

$$Q = \frac{\omega_0}{2\gamma} = \frac{\omega_0}{\Gamma} \quad , \quad \Gamma = 2\gamma \tag{S13}$$

The damped resonance implies a frequency response that follows a Lorentzian shape, hence the response of the resonator (considering a single resonance) is then proportional to

$$\boldsymbol{E_R}, \boldsymbol{H_R}, \boldsymbol{A_R}, \boldsymbol{J_R}, \rho_R \propto \frac{A}{\omega_0^2 - \omega^2 + i\Gamma\omega} \tag{S14}$$

The resonance can be excited by either the probing tip or by an incident free space beam (only for the case of bright resonances), which we can assume to be monochromatic as in the experiment. Let us first consider the case of the free space beam: first, we call $\boldsymbol{E}_{inc}(x, y, z)$ the geometric of the incident beam assuming that no h-BN resonator is present. Note that $\boldsymbol{E}_{inc}(x, y, z)$ includes any reflection from the substrate. If the resonator is instead present, the total field is different and can be called $\boldsymbol{E}_{tot}(x, y, z)$, which can be split in two parts

$$\boldsymbol{E}_{tot}(x, y, z) = \boldsymbol{E}_{inc}(x, y, z) + \boldsymbol{E}_{sc}(x, y, z) \tag{S15}$$

where $\boldsymbol{E}_{sc}$ is the scattered field. A similar decomposition can be done for the $\boldsymbol{H}$ field as well. For small particles, $\boldsymbol{E}_{sc}$ is significant only if the used frequency is close to a resonance, and its geometry is determined by the resonant mode. The scattered field is the superposition of the fields associated to each excited mode

$$\boldsymbol{E}_{sc}(x, y, z, \omega) = \sum\nolimits_n a_n\, \boldsymbol{E}_{M,n}(x, y, z, \omega) = \sum\nolimits_n a_n \frac{A_n}{\omega_{0,n}^2 - \omega^2 + i\Gamma_n\omega} \boldsymbol{E}_{R,n}(x, y, z) \tag{S16}$$

where a_n is the amplitude of the scattered field of the n$^{\text{th}}$ mode, which depends on the coupling between the incident and the mode field geometry $\boldsymbol{E}_R$.

The amplitude a_n of the mode can be computed by choosing a closed surface *S* enclosing the particle and integrating to find the field coupling

$$a_n = A_{inc \to mode} = \frac{\oiint_S (\boldsymbol{E}_{inc} \times \boldsymbol{H}_R^* - \boldsymbol{E}_R^* \times \boldsymbol{H}_{inc}) \cdot \hat{n}\, \mathrm{d}^2 r}{\oiint_S (\boldsymbol{E}_R \times \boldsymbol{H}_R^* - \boldsymbol{E}_R^* \times \boldsymbol{H}_R) \cdot \hat{n}\, \mathrm{d}^2 r} \tag{S17}$$

The integral at the denominator is equal to the total power injected in the mode, which we call P_{MODE}, so we can rewrite it as

$$A_{inc\to mode} = \frac{\oiint_S (\boldsymbol{E}_{inc} \times \boldsymbol{H}_R^* - \boldsymbol{E}_R^* \times \boldsymbol{H}_{inc}) \cdot \hat{n} \mathrm{d}^2 r}{P_{\mathrm{MODE}}} \tag{S18}$$

The relationship still works if an arbitrary value for P_{MODE} is used, provided that the mode fields $\boldsymbol{E}_R$ and $\boldsymbol{H}_R$ are chosen accordingly to the selected power of the mode. Importantly, P_{MODE} can be interpreted as the sum of the radiated power and the dissipated power

$$P_{\mathrm{MODE}} = P_{RAD} + P_{DISS} \tag{S19}$$

Note that P_{RAD} vanishes for dark modes. Similarly, $A_{inc\to mode} = 0$ for dark modes, since the sphere can be selected far from the near field, where the total field is 0. This trivially means that it is not possible to excite dark modes using a beam incident on the sample.

In the used near field setups the sample is scanned while the tip and the beam are still. Mathematically, this is equivalent to keeping the sample and the reference surface S still and moving both the beam and the tip. The focused beam can locally be approximated by a plane wave

$$\boldsymbol{E}_{inc}(x, y, z) \simeq \boldsymbol{E}_0 e^{-i\boldsymbol{k}\cdot\boldsymbol{r}} \tag{S20}$$

If the displacement of the sample due to scanning is $\Delta r = (\Delta x, \Delta y, 0)$ then this is equivalent to changing the phase of the global wave

$$\boldsymbol{E}'_{inc}(x, y, z) = \boldsymbol{E}_{inc}(x - \Delta x, y - \Delta y, z) \simeq \boldsymbol{E}_0 e^{-i\boldsymbol{k}\cdot\boldsymbol{r}} e^{i(k_x x + k_y y)} \simeq e^{i(k_x x + k_y y)} \boldsymbol{E}_{inc}(x, y, z) \tag{S21}$$

$$\boldsymbol{H}'_{inc}(x, y, z) = \boldsymbol{H}_{inc}(x - \Delta x, y - \Delta y, z) \simeq \boldsymbol{H}_0 e^{-i\boldsymbol{k}\cdot\boldsymbol{r}} e^{i(k_x x + k_y y)} \simeq e^{i(k_x x + k_y y)} \boldsymbol{H}_{inc}(x, y, z) \tag{S22}$$

Therefore, by inspection of equation S18, S21 and S22

$$A_{inc\to mode} \propto e^{i(k_x \Delta x + k_y \Delta y)} \tag{S23}$$

This phase shift can be neglected when scanning the considered deep subwavelength resonators, but has to be compensated for larger flakes and guided modes, as done in our previous work (17). Neglecting the phase shift implies

$$A_{inc\to mode} \propto e^{i(k_x \Delta x + k_y \Delta y)} \simeq 1 \tag{S24}$$

Let us now consider the case where light is coupled in the resonator via the AFM tip (which can occur

also for dark resonances where the far field vanishes): the same argument can be used by replacing the incident field of the beam with the field launched by the tip. The tip can be approximated as an Hertzian dipole polarized along z, and the surface S can be chosen an infinitesimal sphere around it. We then express the coupling as

$$A_{tip\to mode} = \frac{\oiint_S \left(\boldsymbol{E}_{tip} \times \boldsymbol{H}_R^* - \boldsymbol{E}_R^* \times \boldsymbol{H}_{tip}\right) \cdot \hat{n} \mathrm{d}^2 r}{P_{\mathrm{MODE}}} \tag{S25}$$

where the Hertzian dipole fields of the tip in spherical coordinates are (in the near field limit $r \to 0$)

$$H_{R,\phi} = i\frac{I\mathrm{d}l}{4\pi}\left(\frac{k}{r} - \frac{i}{r^2}\right)\sin(\theta)\, e^{-i\boldsymbol{k}\cdot\boldsymbol{r}} \to \frac{I\mathrm{d}l}{4\pi r^2}\sin(\theta) \tag{S26}$$

$$E_{R,\theta} = i\frac{\eta I dl}{4\pi}\left(\frac{k}{r} - \frac{i}{r^2} - \frac{1}{kr^3}\right)\sin(\theta)\, e^{-i\boldsymbol{k}\cdot\boldsymbol{r}} \to -i\frac{\eta I dl}{4\pi k r^3}\sin(\theta) \tag{S27}$$

$$E_{R,r} = i\frac{\eta I dl}{4\pi}\left(-\frac{i}{r^2} - \frac{1}{kr^3}\right)\cos(\theta)\, e^{-i\boldsymbol{k}\cdot\boldsymbol{r}} \to -i\frac{\eta I dl}{4\pi k r^3}\cos(\theta) \tag{S28}$$

where η is the free space impedance. On the infinitesimal sphere S the fields of the mode are then constant. It follows that the numerator of equation S25 only depends on the z component of the electric field, and the integral reads

$$A_{tip\to mode} = \frac{\oiint_S \left(-\boldsymbol{E}_R^* \times \boldsymbol{H}_{tip}\right) \cdot \hat{n} \mathrm{d}^2 r}{P_{\mathrm{MODE}}} = \frac{2E_{R,z} I dl}{3P_{\mathrm{MODE}}} \tag{S29}$$

If we take into account the scanning offsets $\Delta x, \Delta y$ we have

$$A_{tip\to mode} \propto E_{R,z}(\Delta x, \Delta y, 0) \tag{S30}$$

In other words, the coupling is proportional to the z component of the electric field of the resonating mode.

Furthermore, we will indicate the coupling between the incident field and the Hertzian dipole as $A_{inc\to tip}$, and we assume it is constant since the tip does not move with respect to the incident field. Because of reciprocity, if light can couple from the tip to the sample, it can also couple back with the same coupling, and more in general

$$A_{1\to 2} = A_{2\to 1} \tag{S31}$$

We can now determine the dependence of the detected signal with respect to the scanning offsets $\Delta x, \Delta y$

to predict the complex map associated to each of the light path described in the main paper (fig. S2).

The *material contrast* is the contribution usually observed with s-SNOM measurement, and hence it is well known and depends solely on the optical constants of the materials immediately below the tip. Hence, since the resonance is not involved, this component can be treated simply as a complex number that, in our problem, takes two values: one on the h-BN nanostructure and the other on the substrate.

The *direct coupling* contribution can occur in two different ways which, however, are equivalent due to equation S31. The total contribution is then

$$A_{\text{direct}} = \sum_n \frac{A_n}{\omega_{0,n}^2 - \omega^2 + i\Gamma_n\omega} A_{inc\to mode(n)}\ A_{mode(n)\to tip}\ A_{tip\to inc} \tag{S32}$$

Only the modes excited directly by the incident wave contribute to equation S32. For instance, the orientation of the polarization of the excited dipole mode is parallel to the polarization of the incident beam. If a single mode n is excited, then the direct contribution reads

$$A_{\text{direct}} \propto \frac{A_n e^{i(k_x\Delta x + k_y\Delta y)}}{\omega_{0,n}^2 - \omega^2 + i\Gamma_n\omega} E_{R,z}(\Delta x, \Delta y, 0) \simeq \frac{A_n}{\omega_{0,n}^2 - \omega^2 + i\Gamma_n\omega} E_{R,n,z}(\Delta x, \Delta y, 0) \tag{S33}$$

In other words, the *direct contribution* is a faithful representation of the z-component of the electric field of the resonant mode.

The *round-trip* contribution is instead given by

$$A_{\text{roundtrip}} = \sum_n \frac{A_n}{\omega_{0,n}^2 - \omega^2 + i\Gamma_n\omega} A_{inc\to tip}\ A_{tip\to mode(n)}\ A_{mode(n)\to tip}\ A_{tip\to inc} \tag{S34}$$

The coupling is mediated exclusively by the tip, so the modes are excited regardless of their orientation with the polarization of the incident field. The obtained image is then

$$A_{\text{roundtrip}} \propto \sum_n \frac{A_n}{\omega_{0,n}^2 - \omega^2 + i\Gamma_n\omega} \left(E_{R,n,z}(\Delta x, \Delta y, 0)\right)^2 \tag{S35}$$

In the case of the disc, if $s > 0$, the cosine and sine modes are always degenerate. Therefore, their squared amplitudes will add together in equation S35, resulting in the expected circularly symmetric patterns

$$(J_s(k_{sn}r + \phi)\cos(s\theta))^2 + (J_s(k_{sn}r + \phi)\sin(s\theta))^2 = \left(J_s(k_{sn}r + \phi)\right)^2 \tag{S36}$$

which in fact does not depend on θ.

The *modulated scattering* contribution is more complex since the presence of the tip can actually modulate all the components of the field, not only the z component. Empirically, we find that this component is negligible, except for the case of the dipole antenna where it appears in the antenna gap. This is because the gap is repeatedly opened and closed by the tip, modulating the overall scattering of the antenna.

The contributions can be separated as explained in the main paper due to the odd symmetry of the dipole modes. This is due to the fact that the incident light is p-polarized, and hence the excited dipole mode will be parallel to the incident polarization. The charge, and hence the z component of the electric field, has opposite values on the two ends of the dipole. Knowing this, one can separate the *direct coupling* contribution (which, being a faithful representation of the field, also has an odd symmetry) by taking the difference between the initial fields and a replica flipped along the odd symmetry axis of the mode. The *round-trip* contribution is instead even, due to the aforementioned dependence on the square of the field, and hence is obtained summing instead of subtracting.

We empirically find that the PiFM displays the *round-trip* contribution of the fields very clearly, as shown in the main paper. However, if the polarization of the incident light is aligned to the dipole antenna, a slight asymmetry can be seen, as evident in fig. S3. This suggests an interference effect between *round-trip* and *direct coupling*, showing that also the *direct coupling* can affect the PiFM.

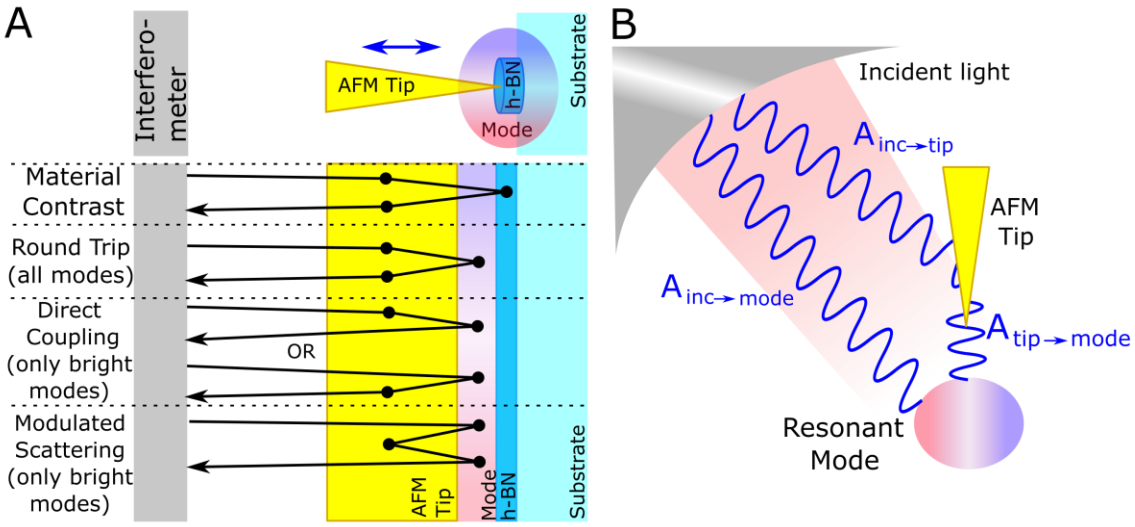

fig. S2. Possible light paths and coupling coefficients. (**A**) Photon paths as in Fig. 3 in main paper. (**B**) Graphical representation of the coupling coefficients $A_{inc\to tip}$, $A_{tip\to R}$ and $A_{inc\to R}$.

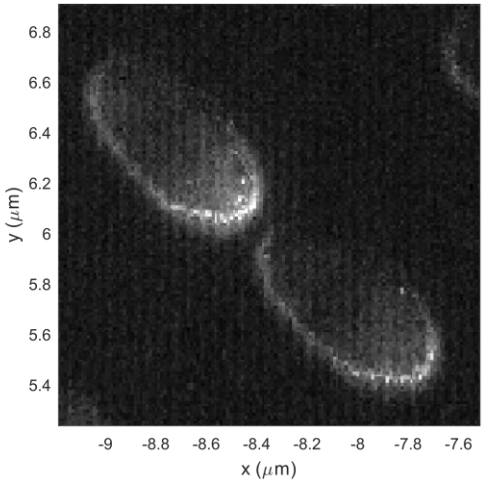

fig. S3. Additional PiFM image of the dipole antenna. PiFM is performed at 1402 cm^{-1}, with the incident field polarized along the antenna.

section S4. Additional measurements

This section provides additional measurements performed on the h-BN nano-discs and antennas.

Figure S4 shows that resonances are also visible in the RS1 band in these nanoparticles. Interestingly, because the propagating polaritons in the RS1 band have negative phase velocity, the smaller particles resonate at a lower photon frequency (fig. S4A-C), and higher order modes appear at lower frequencies (fig. S4D, E).

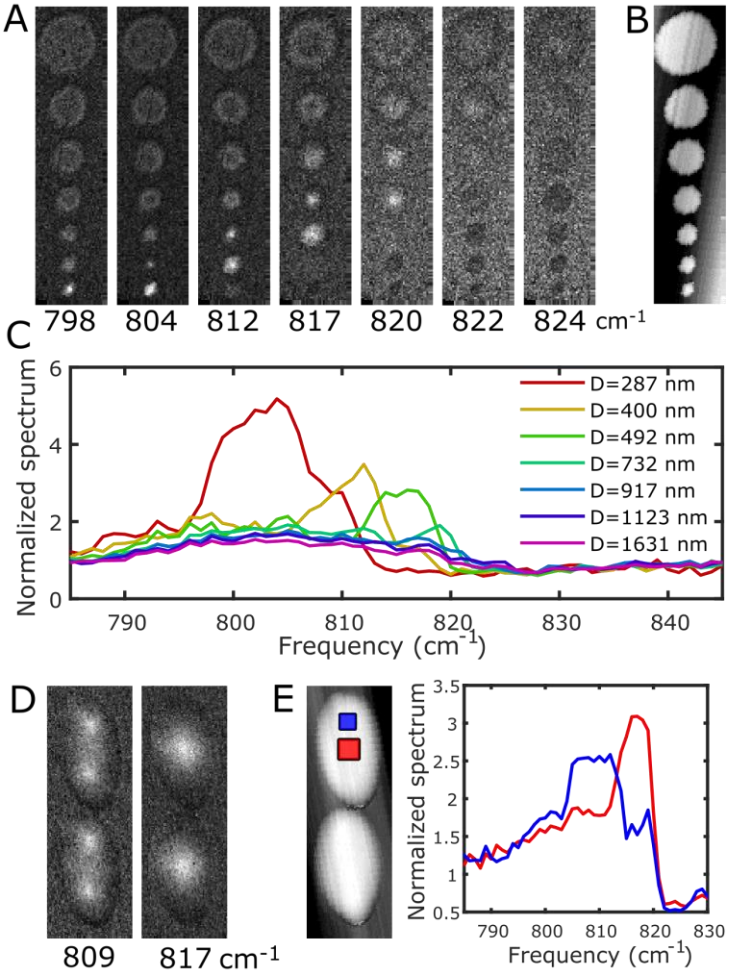

fig. S4. Polaritons in discs and ellipses in the RS1 band. (**A**) Frequency slices of a hyperspectral scan taken on an array of discs in the RS1 band. Because guided modes in h-BN have a negative effective index in the RS1 band, smaller discs resonate at lower frequencies, which is the opposite of the usual behavior of polaritons. Disc diameters are 1630, 1120, 920, 730, 490, 400 and 290 nm. (**B**) Topography for the discs in A. (**C**) Spectra taken at the center of each disc. The PiFM signal is much stronger for smaller resonators, in agreement with the fact that PiFM signal is proportional to the gradient of the optical force, which is much larger in smaller structures. (**D**) The negative effective index also causes higher order modes in the nanoantennas to appear at lower frequencies. (**E**) Topography of the particles and the spectrum in two different positions.

Movies S1 to S4 show the full hyperspectral PiFM characterization of the nanoparticles and nano-antennas. Each frame of the movie corresponds to a frequency (indicated in the title of the frame above the image). More specifically:

- **movie S1. Hyperspectral PiFM for different wavelengths in the RS1 band.** Is an overview of all the fabricated nanostructures for different wavelengths in the RS1 band
- **movie S2. Hyperspectral PiFM for different wavelengths in the RS2 band.** Is an overview of all the fabricated nanostructures for different wavelengths in the RS2 band
- **movie S3. Zoom-in hyperspectral PiFM for different wavelengths in the RS1 band.** Is a zoom-in on the dipole antennas and smallest nanoparticles for different wavelengths in the RS1 band

- **movie S4.**). **Zoom-in hyperspectral PiFM for different wavelengths in the RS2 band.** is a zoom-in on the dipole antennas and smallest nanoparticles for different wavelengths in the RS2 band

Figure S5 shows a comparison of s-SNOM optical images and PiFM images taken on the same setup, with the same illumination conditions. This was possible by implementing PiFM on the Neaspec setup via modulation of the CW QCL laser. It can be seen that the PiFM signal is very similar with respect to the amplitude of the second harmonic of the optical fields, demonstrating the common origin of the observed polariton images.

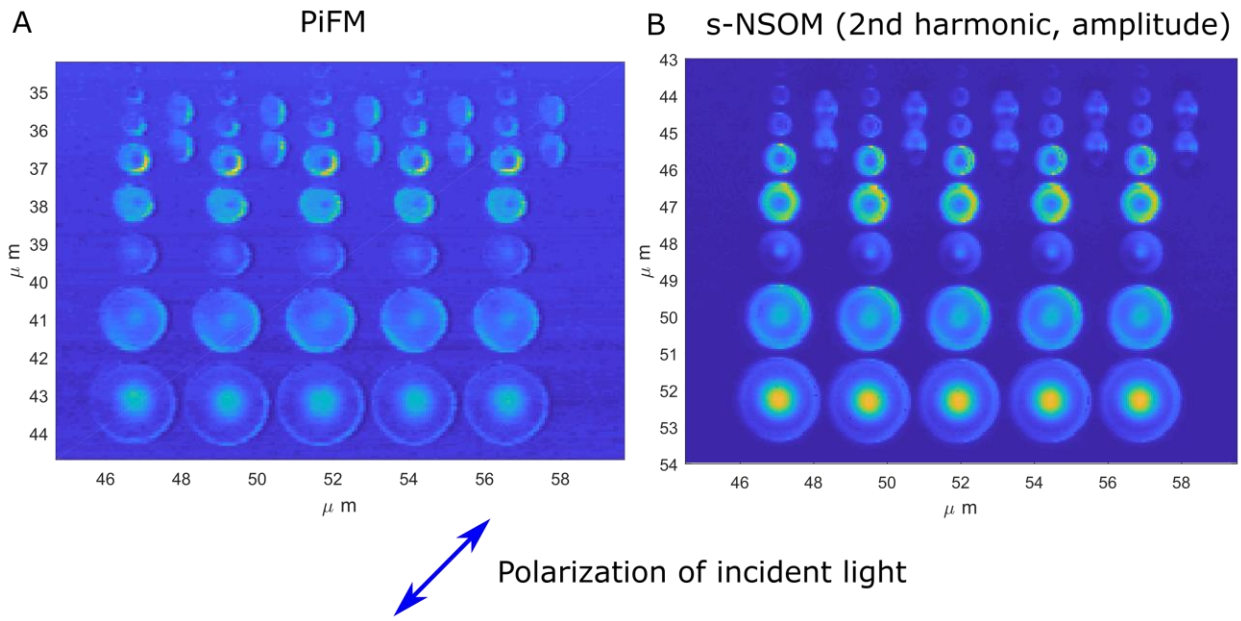

fig. S5. Comparison of PiFM and s-SNOM on the same setup (Neaspec). (**A**) PiFM. (**B**) s-SNOM using the second harmonic, amplitude is plotted. Both measures have been performed at 1410 cm^{-1}.

Figure S6 shows the resonances in a disc that has been moved with respect to its initial position, demonstrating that the resonances are supported by the h-BN disc itself. The resonances are the same in an identical disc still in its original position.

Finally, fig. S7 shows additional measurement performed on the nanoparticles using PiFM with monochromatic excitation (while the images shown in the main paper are hyperspectral).

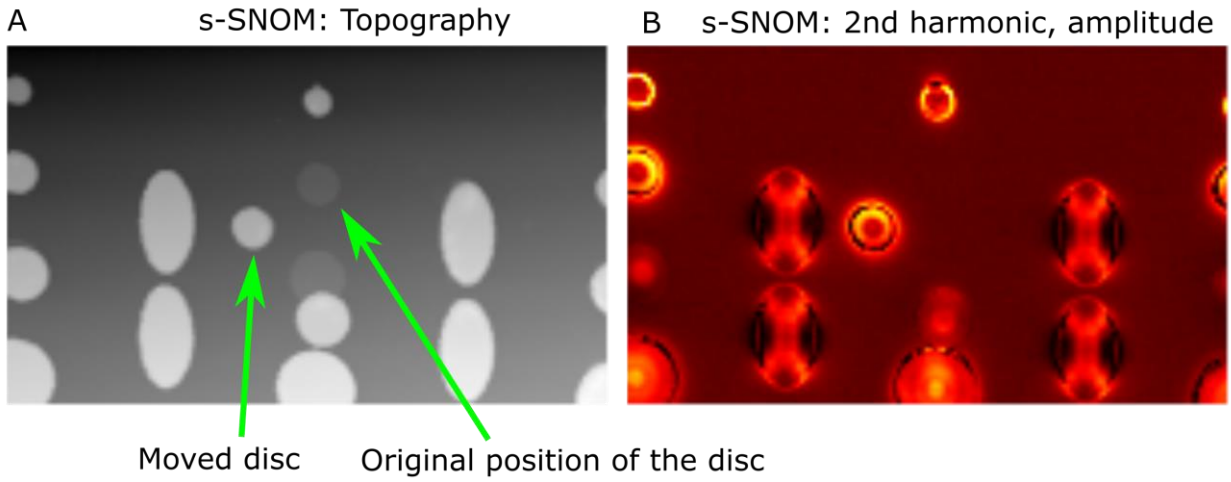

fig. S6. Resonance in a disc shifted from its original position. (**A**) Topography. The original position of the disc is still visible due to the fact that during fabrication the SiO_2 substrate is partially etched outside of the resist mask, leaving a pedestal under the disc. The moved disc can be used to determine the actual thickness of h-BN. (**B**) Resonances imaged with s-SNOM (1455 cm^{-1}) using the second harmonic.

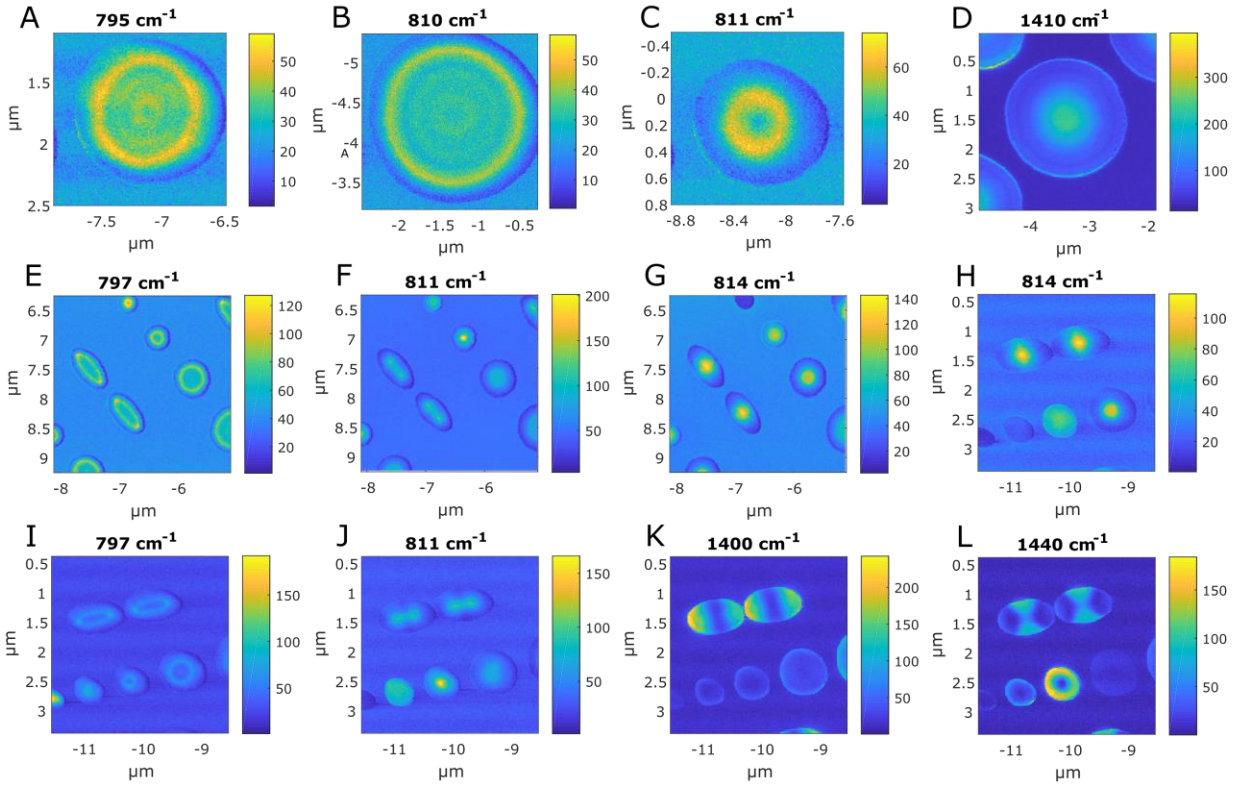

fig. S7. Monochromatic PiFM images. (**A-C**) Single nanoparticles in the RS1 band. (**D**) Single nanoparticle in the RS2 band. (**E-J**) Overview of several nanoparticles in the RS1 band. (**K**, **L**) Overview of several nanoparticles in the RS2 band, with the first two dipole modes.

section S5. Numerical simulations of Purcell factors

Purcell factors are computed directly from the power radiated by a dipole source, and are shown in tables S1 and S2:

table S1. Purcell factors for nanodiscs. Numerical calculations of Purcell factors F_P for 50 nm thick nano-discs with variable diameters. The factors have been computed 50 nm away from the nano-disc edge.

Radius	Resonant λ_0	F_P
290 nm	6.77 um	12000
400 nm	6.85 um	8000
490 nm	6.90 um	6800
730 nm	7.02 um	3800

table S2. Purcell factors for nanoantennas. Numerical calculations of Purcell factors F_P for the dipole nanoantenna presented in the paper, for variable gap sizes. The factors have been computed at the center of the antenna gap.

Gap	Resonant λ_0	F_P
150 nm	7.10 um	4000
100 nm	7.11 um	10000
50 nm	7.12 um	80000